Research Article | Vol. 27, No. 7 | 1 Apr 2019 | OPTICS EXPRESS 9684
Optics EXPRESS

Performance analysis of distributed optical fiber acoustic sensors based on φ-OTDR

MENGMENG CHEN,[1,2] ALI MASOUDI,[2,*] AND GILBERTO BRAMBILLA[2]

[1]School of Electronics and Engineering, Nanjing Xiaozhuang University, Nanjing 211171, China
[2]Optoelectronics Research Centre, University of Southampton, Southampton, SO17 1BJ, United Kingdom
*a.masoudi@soton.ac.uk

Abstract: The performance of distributed optical fiber acoustic sensor as a function of parameters such as the linewidth of the laser, the probe pulse width, and the amplitude and frequency of perturbation is experimentally studied. The aim of this study is to experimentally confirm the outcome of the simulation results obtained previously. It is shown that the experimental and simulation results are in good agreement, and the precision of the sensing system depends on the pulse width and linewidth of the probe pulse, as well as the frequency and amplitude of the perturbation. It is shown that the sensing precision of the system can be enhanced by reducing the width of the probe pulse while increasing the linewidth of the laser.

1. Introduction

Phase optical time domain reflectometry (φ-OTDR), which has been used as a distributed acoustic sensor (DAS), was first proposed by Dakin et al. in 1990 [1]. The principle of φ-OTDR is based on acquiring the coherent backscattered Rayleigh light from the sensing fiber and extracting the phase information of the backscattered light through different schemes [2–4]: for any given section of the fiber, the phase-difference between the backscattered light from the two ends of that section is a linear function of the length of the section [5–7]. By monitoring the phase variation of the backscattered light from the two ends of each section, the strain distribution along the fiber can be quantified. There are many methods to evaluate the phase in φ-OTDR [8]: such as dual pulse method [7,9-10], heterodyne detection [11], homodyne detection [12], direct detection using chirped pulse as probe signal [13,14], and interferometric phase recovery method [6,15]. This paper focuses on φ-OTDR based on interferometric phase recovery.

In interferometric DAS systems, the backscattered light from a single pulse is launched into an imbalanced Michelson or Mach-Zehnder interferometer, with two unequal arms to provide two similar traces with a temporal shift of ΔT. The two temporally shifted traces are then mixed and the differential phase information at any given section of the sensing fiber is extracted by a phase demodulation algorithm.

Since 2013, a series of systematic studies have been carried out on interferometric DAS systems [6,16–21]. In 2013, Masoudi et al. used an imbalance Mach-Zehnder interferometer (IMZI) to quantify the vibrations along a 1 km long sensing fiber [6]. The system sensitivity was later improved through a novel optical arrangement by using a single narrow fiber Bragg grating (FBG) filter to reduce the amplified spontaneous emission (ASE) for both fiber amplifiers and an improved signal processing procedure that was less susceptible to noise [17]. In 2015, Fang et al. adopted a different approach to realize a DAS system by using an imbalanced Michelson interferometer combined with phase-generated carrier (PGC) demodulation algorithm. In 2017, two numerical models were developed to analyze interferometric DAS systems [18,19]. The two studies provided an insight into the operation and the limitations of such systems. More recently, DAS systems based on few-mode and

#355688 https://doi.org/10.1364/OE.27.009684
Journal © 2019 Received 18 Dec 2018; revised 4 Feb 2019; accepted 4 Feb 2019; published 21 Mar 2019

Optics EXPRESS

multimode fibers have been demonstrated [20,21]. Murray et al. used off-axis holography with a high-speed camera to record and analyze the entire backscattered light, making the system immune to signal fading [20]. Chen et al. instead separate the backscattered light from different modes using a mode multiplexer and analyze the backscattered light from each mode individually [21].

The numerical model used to analyze the behavior of interferometric DAS system showed that the sensing system has a higher sensing precision for dynamic strains with lower amplitude and higher frequency [18]. Furthermore, the precision of the sensing system as a function of the pulse width and linewidth of the probe pulse showed that the precision of the measurement can be increased by reducing the probe pulse width or by increasing the laser linewidth. In this study, the performance of DAS based on an IMZI is experimentally analyzed. The effect of the parameters such as the laser linewidth, the probe pulse width, and the vibration amplitude and frequency on the sensing system sensitivity are studied and juxtaposed with the numerical assessment of reference [18].

2. Principle

A φ-OTDR system relies on the phase of the backscattered light to spatially resolve the strain level at each point along the sensing fiber. The layout of a typical interferometric DAS used for phase analysis is shown in Fig. 1. In this arrangement, the phase information is extracted by splitting and launching the backscattered light into two unequal arms of a MZI and recombining the temporally shifted backscattered light with the original one to mix the light from two different points in the fiber. The 3 × 3 coupler at the output of the interferometer is used to avoid phase signal fading. For a single wavelength, λ, the intensity at each port of the 3 × 3 coupler is given by [18]:

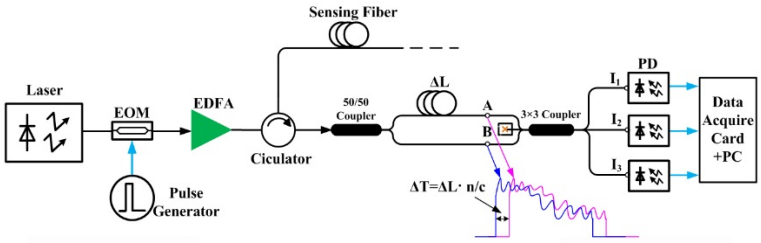

Fig. 1. The outline of a typical interferometric DAS setup.

$$\begin{cases} I_1 = E_A(\lambda)^2 + E_B(\lambda)^2 + 2E_A(\lambda)E_B(\lambda)cos\left[\varphi_A(\lambda) - \varphi_B(\lambda) - \frac{2\pi}{3}\right] \\ I_2 = E_A(\lambda)^2 + E_B(\lambda)^2 + 2E_A(\lambda)E_B(\lambda)cos\left[\varphi_A(\lambda) - \varphi_B(\lambda)\right] \\ I_3 = E_A(\lambda)^2 + E_B(\lambda)^2 + 2E_A(\lambda)E_B(\lambda)cos\left[\varphi_A(\lambda) - \varphi_B(\lambda) + \frac{2\pi}{3}\right] \end{cases} \quad (1)$$

where E_A and E_B, and φ_A and φ_B are the values of the electric field and the phase information at points A and B, respectively (Fig. 1) and λ is the wavelength of the laser. For a non-ideal laser with a broader linewidth, the output intensity at the output of the interferometer can be calculated by integrating of the backscattered intensities over the probe pulse linewidth:

Optics EXPRESS

$$\begin{cases} I_1 = \int_{\lambda_0}^{\lambda_n} \left\{ E_A(\Lambda)^2 + E_B(\Lambda)^2 + 2E_A(\Lambda)E_B(\Lambda)\cos\left[\varphi_A(\Lambda) - \varphi_B(\Lambda) - \frac{2\pi}{3}\right] \right\} d\Lambda \\ I_2 = \int_{\lambda_0}^{\lambda_n} \left\{ E_A(\Lambda)^2 + E_B(\Lambda)^2 + 2E_A(\Lambda)E_B(\Lambda)\cos\left[\varphi_A(\Lambda) - \varphi_B(\Lambda)\right] \right\} d\Lambda \\ I_3 = \int_{\lambda_0}^{\lambda_n} \left\{ E_A(\Lambda)^2 + E_B(\Lambda)^2 + 2E_A(\Lambda)E_B(\Lambda)cos\left[\varphi_A(\Lambda) - \varphi_B(\Lambda) + \frac{2\pi}{3}\right] \right\} d\Lambda \end{cases} \quad (2)$$

Therefore, each measurement includes the superposition of the phase changes of all the wavelengths present in the probe pulse.

To analyze the performance of such system, the parameters that determine the phase of the backscattered light should be studied. Phase change along an optical fiber can be explained with the help of Fig. 2. It shows the distribution of inhomogeneities in two fixed sections of the fiber before and after elongation. The top diagram shows a section of the fiber corresponding to the sensing system gauge length l. The boundaries of the gauge length are distinguished by two rectangles with a width W corresponding to the length of the fiber covered by the probe pulse. The phase of the backscattered light from each rectangular section is determined by the distribution of the inhomogeneities within that section. For an unperturbed fiber, the phase-difference between the backscattered signals from the two sections is:

$$\Delta\varphi = \frac{2\pi n}{\lambda} 2l \times 0.78 + \varphi_2 - \varphi_1 \quad (3)$$

where φ_1 and φ_2 are two random phases and n is the refractive index of the fiber.

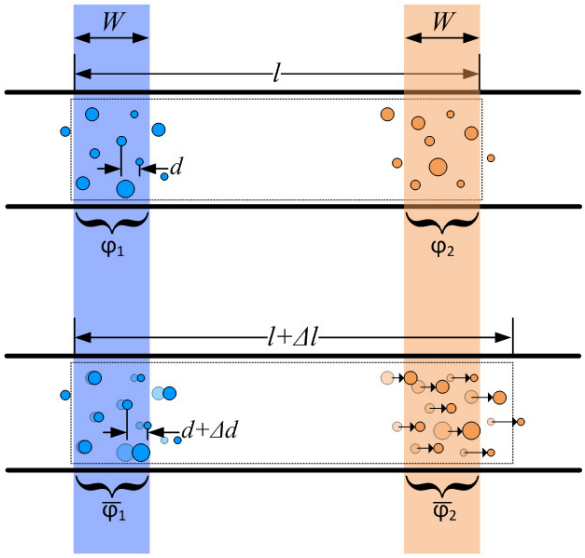

Fig. 2. Distribution of inhomogeneity along two fixed sections of the sensing fiber before and after longitudinal elongation.

The diagram at the bottom of Fig. 2 shows a scenario where the fiber is longitudinally stretched by Δl. This change in the fiber length results in a redistribution of inhomogeneities within each section which in turn leads to a variation in the phase-difference between the

Optics EXPRESS

backscattered light from the two sections. Following the redistribution, the value of the phase-difference, $\overline{\Delta\varphi}$, is given by:

$$\overline{\Delta\varphi} = \frac{2\pi n}{\lambda} 2\left(l + \Delta l\right) \times 0.78 + \overline{\varphi_2} - \overline{\varphi_1} \tag{4}$$

where $\overline{\varphi_1}$ and $\overline{\varphi_2}$ are the phases of the backscattered light from the same stretch of fiber after elongation. The variation in the phase-difference can be obtained by comparing Eqs. (3) and (4):

$$\Delta\Phi = \overline{\Delta\varphi} - \Delta\varphi = \frac{2\pi n}{\lambda} 2(\Delta l) \times 0.78 + \left(\overline{\varphi_2} - \varphi_2\right) + \left(\overline{\varphi_1} - \varphi_1\right) \tag{5}$$

The first term in Eq. (5) represents the linear change in the phase-difference while the other two terms correspond to non-linear changes. Equation (5) shows that linear changes in the phase-difference is directly proportional to the strain level. The non-linear terms appear due to redistribution of scatterers within the two sections from which the phase of the backscattered light is measured. Figure 2 shows that, as the fiber stretches, the relative distance between the inhomogeneities within each section changes from d to $d + \Delta d$. This relative shift results in a random phase variation between $\overline{\varphi_2}$ and φ_2 as well as $\overline{\varphi_1}$ and φ_1.

3. Experimental setup

The experimental setup used to analyze the performance of an interferometric DAS system as a function of parameters such as laser linewidth and probe pulse duration is shown in Fig. 3. A distributed feedback (DFB) laser diode (λ = 1550.12 nm, $\Delta\lambda$ = 2 MHz) was modulated by an electro-optic modulator (EOM) to generate probe pulses. The microwave generator was used to control the linewidth of the DFB laser through direct modulation. The probe pulse was amplified by an erbium-doped fiber amplifier (EDFA1) to raise its peak power to 2.4 W followed by a dense wavelength division multiplexing (DWDM) filter (Filter1: λ_0 = 1550.52 nm; $\Delta\lambda$ = 100 GHz) to eliminate the ASE from the EDFA1. The amplified pulse was passed through an acousto-optic modulator (AOM) (insertion loss = 3.4 dB; extinction ratio = 50 dB). The AOM was synchronized with the EOM to ensure that the amplified pulse from the EDFA1 passes through the AOM in the allotted slot to reach the sensing fiber. The role of the AOM is to suppress the ASE from the EDFA1 [22]. The probe pulse with a peak power of 1.2 W was then launched into the sensing fiber via a circulator C. The sensing fiber consisted of a 6 m long single-mode fiber wrapped around one piezoelectric ceramic (a tube PZT 155 mm in diameter). A 405 m and a 41 m long unstrained–unheated sections of fiber were added before and after the PZT, respectively. The backscattered Rayleigh signal was collected by the circulator C and amplified by the second optical amplifier (EDFA2) and its ASE was filtered by a similar DWDM filter (Filter 2). The filtered light was then fed into the thermally insulated IMZI with path imbalance of 4 m using a 50/50 coupler. Three photodetectors (40 kΩ transimpedance; 125 MHz bandwidth) were used to detect the light from the 3 × 3 coupler at the output of the IMZI. The photodetectors were sampled using a 250 MHz oscilloscope at a sampling rate of 1.25 GSa/s.

Optics EXPRESS

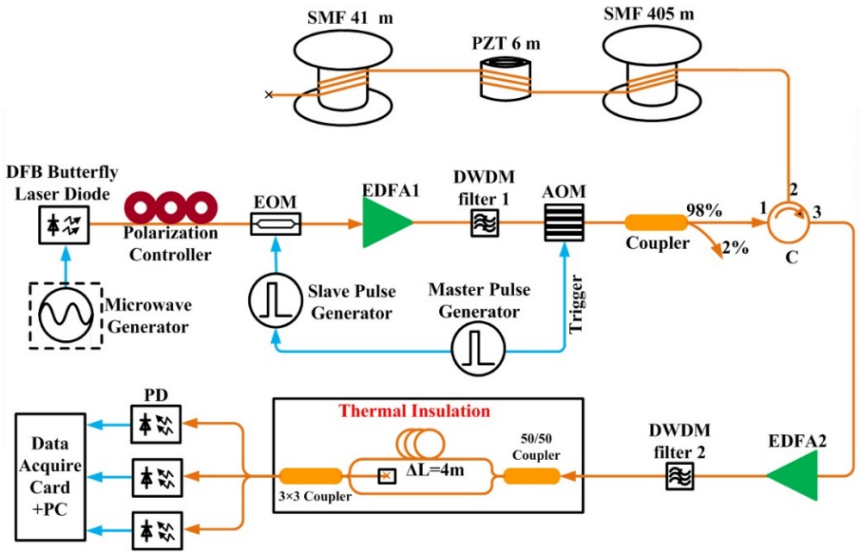

Fig. 3. Experimental setup. DFB, distributed feedback; EOM, electro-optic modulator; EDFA, erbium-doped fiber amplifier; AOM, acousto-optic modulator; C, Circulator; DWDM, Dense Wavelength Division Multiplexing; PD, photodetector.

4. Experimental procedure

First the relationship between the amplitude of the microwave generator and the linewidth of the laser was studied. For this assessment, different modulation voltages V_{pp} from 50 mV to 600 mV with 50 MHz modulation frequency were applied to the DFB laser to generate different linewidths. The linewidth of the directly modulated DFB laser was measured by mixing its output with a highly stable narrow linewidth tunable laser source (TLS). The wavelength of the TLS was tuned to generate a 5GHz intermediate frequency (IF) as it mixed with the output of the DFB laser. This light source was later used to analyze the effect of the linewidth on the precision of DAS systems.

To evaluate the effect of laser linewidth on the precision of the sensor, the behaviour of the system was assessed for five different linewidths between 10 MHz and 1 GHz. For all five linewidths in this analysis, the same parameters were used for the input signal to the PZT (a 1kHz sinewave with $10V_{pp}$), the width of the probe pulse (set to 20ns), and the path imbalance of the IMZI (set to 4m).

To assess the relationship between the probe pulse width and the measurement precision, the EOM was modulated to generate seven different pulse durations from 5 ns to 20 ns. The frequency and amplitude of the input signal to the PZT were kept at 1 kHz and 10 V_{pp}, respectively, while the path-imbalance of the IMZI was kept constant at 4m. A 2 MHz linewidth was used for the laser for this set of tests.

The effect of the perturbation frequency and amplitude on the sensor precision was evaluated by assigning a fixed value to all of the parameters in the sensing system while stepping the frequency and amplitude of perturbations through a range of values. To examine the effect of strain, ten different strain levels from 1 V to 10 V were applied to the PZT at 1 kHz frequency. The effect of frequency was studied by stepping the perturbation frequency from 250Hz to 2000Hz at a fixed input voltage of 4 V. For both sets of analysis, the pulse duration and the probe pulse linewidth were set to 20 ns and 2 MHz, respectively.

5. Experimental results

Figure 4 shows the relationship between the amplitude of the microwave generator and the linewidth of the DFB laser directly modulated by the microwave generator. Figure 4(a) shows

Optics EXPRESS

the laser frequency spectrum for four different modulation voltages, from 50 mV to 350 mV. Figure 4(b) shows the relationship between laser linewidth and the modulation amplitude. The blue dashed line in this Fig. represents the regression line fitted to the data points and has a R^2 value of 0.969. Here, R^2 is defined as the coefficient of determination.

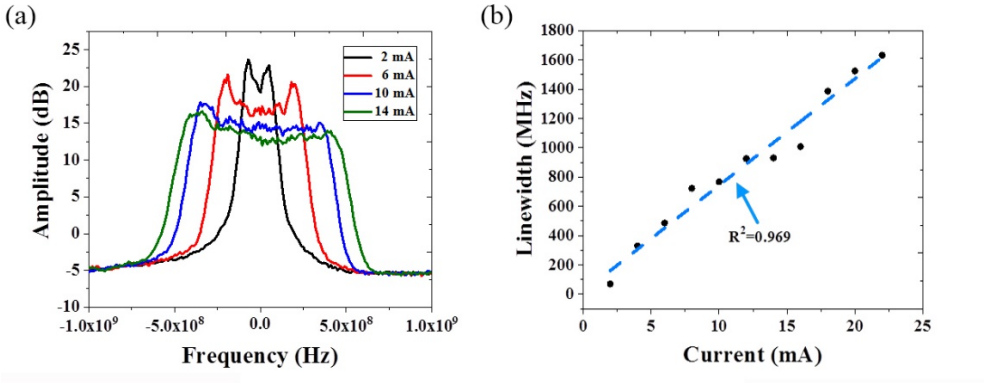

Fig. 4. Linewidth of the directly modulated DFB laser. (a) The frequency spectrum of the DFB laser for different modulated voltages, (b) Relationship between the linewidth of the laser and the amplitude of the modulation signal.

The time domain backscattered traces from the sensing fiber probed by probe pulses with 10 MHz and 1 GHz linewidths are shown in Fig. 5. The blue and orange traces show the OTDR trace for the 10 MHz-linewidth and 1 GHz linewidth sources, respectively.

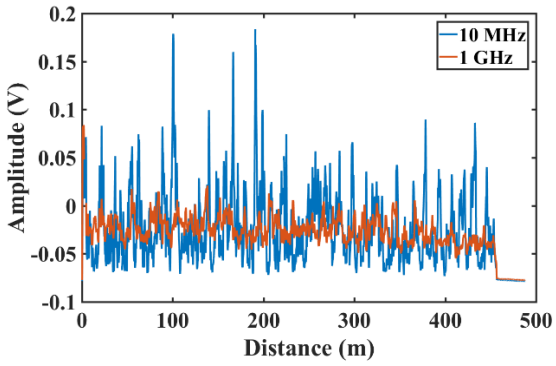

Fig. 5. Time domain Rayleigh backscattered traces for a probe pulse with 10 MHz linewidth (in blue) and 1 GHz linewidth (in orange).

The 3D diagram of Fig. 6 demonstrates the output of the sensing system for 1 kHz vibration with an amplitude of 10 V_{pp} for a laser with 500 MHz linewidth. The phase was extracted from the intensity of the Rayleigh backscattered light using arc-tangent demodulation procedure [17]. According to this procedure, the phase-difference between two adjacent sections of the sensing fiber is given by [17]:

$$\Delta\phi = \arctan\left(\frac{\dot{I}_2 - \dot{I}_3}{\dot{I}_1}\right) \tag{6}$$

where $\dot{I}_1, \dot{I}_2$ and $\dot{I}_3$ are the AC components of the intensities at the three detectors.

Figure 6(a) shows the output of the system in time domain. The two horizontal axes represent the distance along the fiber and time while the vertical axis represents the strain

Optics EXPRESS

amplitude. Figure 6(b) shows the system output in frequency domain. This diagram was obtained by calculating the Fourier transform of the results in time-domain at each point on the sensing fiber.

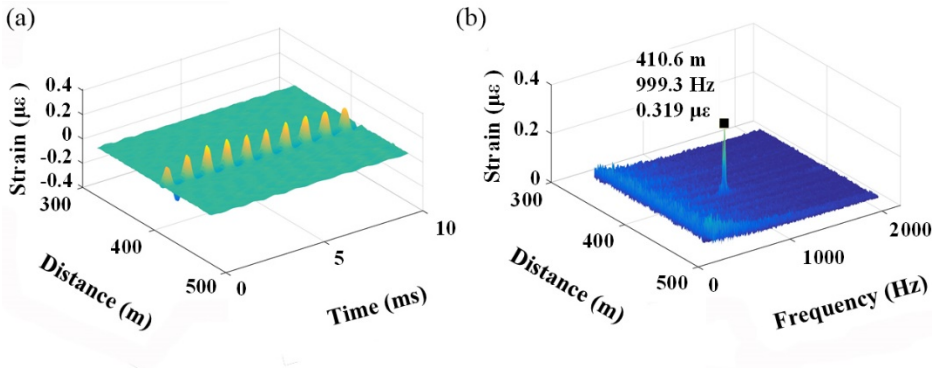

Fig. 6. 3D representation of the strain distribution along the fiber for a 1 kHz vibration with an amplitude of 10 V_{pp} and a probe pulse linewidth of 500 MHz. The graphs represent 3D maps of the strain distribution (a) in the time domain, and (b) in the frequency domain.

Figure 7 shows the standard deviation (SD) of the strain measurement carried out by DAS as a function of the linewidth of the probe pulse. For each data point, the SD is obtained by calculating the root mean square (RMS) of 600 data points from eight different measurements (each measurement interrogates the strain rate along a 6 m long fiber wrapped around the PZT. With 1.25 GSa/s sampling rate, each measurement yields 75 data points). The dashed line in the graph represents the logarithmic line fitted to the data points and has a R^2 value of 0.9795. The horizontal axis of this diagram is plotted in logarithmic scale to better clarify the relationship between the probe pulse linewidth and the results standard deviation.

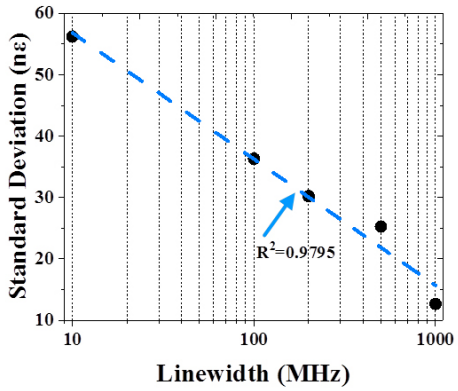

Fig. 7. Relationship between the SD of the strain level measured by using φ-OTDR and the probe pulse linewidth. For this diagram, the sensing system was set for a range of linewidths from 10 MHz to 1 GHz for a fixed pulse width of 2m.

Figure 8 demonstrates the relationship between the SD and the strain measurement carried out by the DAS system as a function of the probe pulse duration. The blue dashed line in this Fig. determines the regression line fitted to the data points. The SD for each pulse duration was obtained by calculating the RMS of 600 data points from eight different measurements and has a R^2 value of 0.9378.

Optics EXPRESS

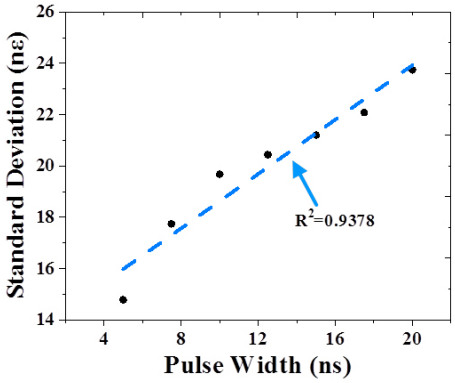

Fig. 8. Relationship between the SD of the strain level measured by using φ-OTDR and the probe pulse width. For this diagram, the sensing system was set by stepping the pulse widths from 50 cm to 2 m in 25 cm steps while the probe pulse linewidth was fixed to 2 MHz.

Figure 9 shows the strain response of the system to 1 kHz sinusoidal strain at various strain levels. Figure 9(a) exhibits the measurement results carried out by the DAS system as a function of the input voltage. Each data point in this Fig. is the average of 600 data points from eight different measurements. The error bar assigned to each data point represents the SD of the experimental results at each strain level. The blue dashed line in this Fig. represents the regression line fitted to the data points. Figure 9(b) illustrates the SD of the data points shown in Fig. 9(a). The blue dashed line in this Fig. also represents the linear line fitted to the data points and has a R^2 value of 0.9941.

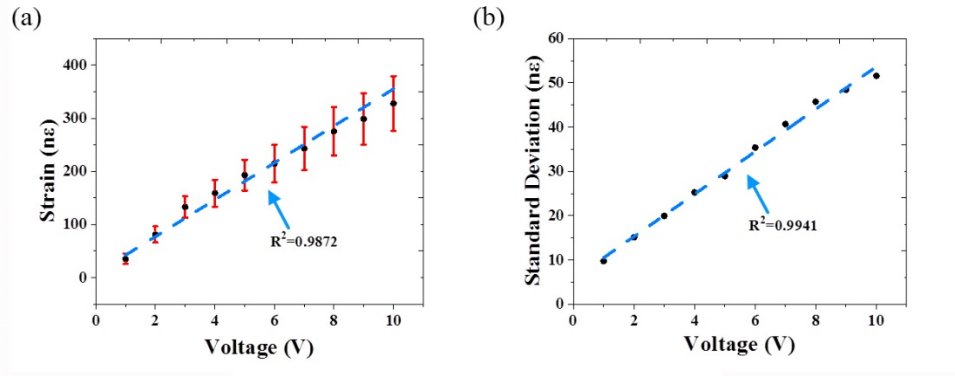

Fig. 9. System response to a 1 kHz sinusoidal strain ranging from 50 nε to 350 nε. (a) Experimental results as a function of the induced strain amplitude, (b) SD of different realization of the system model versus the induced strain amplitude.

Figure 10 shows the behaviour of the sensing system to a fixed strain level at different frequencies. Figure 10(a) exhibits the output (blue points) of the φ-OTDR system to 4V sinusoidal strains at different frequencies ranging from 250 Hz to 2000 Hz: the strain response of PZT is different to different frequencies, as seen from the red line. In line with the previous assessments, the data for each frequency value was obtained by averaging the results from 600 data points from eight different measurements. The error bar assigned to each data point represents the SD of those individual realizations. Figure 10(b) illustrates the relationship between the frequency of the induced strain and the standard deviations of the data points in Fig. 10(a): the blue dashed line in this Fig. represents the regression line fitted to the data points and has a R^2 value of 0.8843.

Optics EXPRESS

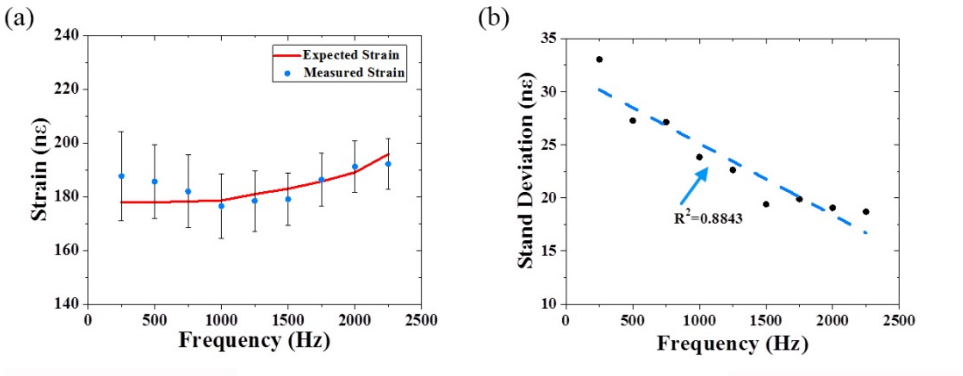

Fig. 10. System response to 4 V perturbations for a frequency ranging from 250 Hz to 2250 Hz. (a) System output as a function of the frequency of the induced strain, (b) SD of different realization of the system versus the frequency of the induced strain.

6. Discussion

Figure 4 shows that the laser linewidth can be adjusted through the injected voltage. The increase in the linewidth of the laser at higher modulation voltages can be clearly observed in Fig. 4(a). Figure 4(b) demonstrates that for the DFB laser used in this experiment, the modulation amplitude has a linear relationship with the linewidth with a slope of 2.91 MHz/mV. In Fig. 5, the backscattered trace for a probe pulse with 1 GHz linewidth shows much lower coherent Rayleigh noise compared with that of a probe pulse with 10 MHz linewidth. This observation agrees with both the simulation results and the theory [18].

The location of the sinusoidal oscillation on the 3D diagram of Fig. 6(a) matches the location where the sensing fiber was attached to the PZT. Moreover, the frequency and amplitude of the oscillation agree with that of the input voltage to the PZT. This figure clearly shows the capability of the sensing system in localizing the position of the perturbation without any cross-talk between the perturbed and unperturbed region. The peak in the 3D plot of Fig. 6(b) corresponds to the frequency and strain applied by the PZT at 410 m and demonstrates that the sensor can measure the location, frequency, and strain of dynamic perturbations along the fiber.

The results in Fig. 7 indicate that the precision of the strain measurement has a logarithmic relationship with the laser linewidth. This relationship can be explained with the help of Eqs. (2) and (5). By combining the two equations, the intensity at one of the three detectors is given by:

$$I=\int_{\lambda_0}^{\lambda_n} E_A(\Lambda)^2+E_B(\Lambda)^2+2E_A(\Lambda)E_B(\Lambda)\cos\left(\frac{2\pi n}{\Lambda}2l\times 0.78+\varphi_2(\Lambda)-\varphi_1(\Lambda)\right)d\Lambda. \quad (7)$$

With an assumption that the spectral attenuation of the fiber is flat over the linewidth of the laser and by neglecting the loss over the gauge length, the intensity at the detector can be estimated by:

$$I=2E^2\int_{\lambda_0}^{\lambda_n}\left[1+\cos\left(\frac{2\pi n}{\Lambda}2l\times 0.78+\varphi_2(\Lambda)-\varphi_1(\Lambda)\right)\right]d\Lambda. \quad (8)$$

where $E_A(\Lambda)=E_B(\Lambda)=E$. This equation shows that the first term in the cosine function has a linear contribution to the phase measurement for all of the wavelengths present in the linewidth of the laser. On the other hand, the last two terms in the cosine function, $\varphi_2(\Lambda)-\varphi_1(\Lambda)$, have a random value at different wavelengths. By integrating the phase-

Optics EXPRESS

difference between two points of the fiber over the linewidth of the laser, the first term in phase of the cosine function will have uniform contribution for all the wavelengths while the effect of the second term will diminish due to its random nature.

It should be pointed out that the linewidth of the seed laser cannot be increased indefinitely to achieve a better precision as the broader linewidth reduces the coherent Rayleigh noise (CRN) of the backscattered light. For a system with a spatial resolution of Δz , the standard deviation of the CRN as a fraction of the Rayleigh signal is given by [23]:

$$f_{CRN} \simeq \left(\frac{V_g}{4 \Delta z \Delta \nu} \right)^{\frac{1}{2}} \tag{9}$$

where V_g is the group velocity and $\Delta \nu$ is the source linewidth in hertz. This Eq. shows that a seed laser with a broader linewidth results in a backscattered trace with a lower CRN. Since the vibration measurement relies on the changes in the intensity of light at the detectors, using a light source with a broad linewidth reduces the strain resolution of the sensor.

Figure 8 shows that the standard deviations of the strain levels obtained from the experimental results have a linear relationship with the duration of the probe pulse. The linear relation between the pulse width and the SD can be explained with the help of Eq. (5). The first term in this equation, $2\pi n / \lambda \cdot 2\Delta l$, has a linear relationship with the fiber elongation while the other two terms vary in a non-linear fashion. As a result, the strain-elongation transfer function is not quite linear, and the level of the non-linear changes depends on which extent the inhomogeneities within the width of the probe pulse are displaced relatively to one another as the fiber stretches. When a long probe pulse is used for interrogation, it covers a longer section of the fiber and, hence, more scattering points. Therefore, even a low strain level can have a significant effect on $\left(\overline{\varphi_1} - \varphi_1\right)$ and $\left(\overline{\varphi_2} - \varphi_2\right)$ as illustrated in Fig. 2. For a short probe pulse, on the other hand, the relative displacement of the scatterers is small, since the pulse covers a shorter fiber section. Therefore, the redistribution of the scatterers does not significantly affect the phase of the backscattered light from that section.

Although the precision of the measurement can be increased by reducing the width of the probe pulse, a pulse with a shorter duration results in a weaker backscattered light and, consequently, lower system sensitivity. Therefore, there is a trade-off between the measurement precision and the duration of the probe pulse.

Figure 9(a) shows a linear relationship between the induced and measured strain. Figure 9(b) shows that the SD of the output has a linear relationship with the level of the induced strain. This response can be explained with the help of Fig. 2. This relative shift results in disproportionate phase variation between $\overline{\varphi_2}$ and φ_2 as well as $\overline{\varphi_1}$ and φ_1. For a small strain level, the relative shift between scatterers is negligible, therefore the deviation in $\Delta\varnothing$ is small, whereas for a large strain level, the relative shift between scatterers is much more significant and, as a result, the deviation in $\Delta\varnothing$ becomes much larger. Consequently, the deviation starts to increase as the strain level increases, and this correlation can be observed in Fig. 9(b).

Figure 10 demonstrates that the DAS system used in this experiment has approximately a flat frequency response from 250 Hz to 2500 Hz. The graph shows that the error bar of each data point covers the expected value of the response. Figure 10(b) shows that low frequency perturbations have a higher SD compared with higher frequency perturbations. For any periodic signal, the precision of the measurement is proportional to the number of cycles sampled. For a high frequency perturbation, the signal processing procedure takes advantage of the data acquired over several cycles to evaluate the strain level. For low frequency perturbation, fewer cycles can be sampled during the same period. Therefore, the sensing system demonstrate a lower SD for higher frequency perturbations.

Optics EXPRESS

Furthermore, the reduction in the SD cannot be fully linked to the frequency response of the PZT. According to Fig. 10(a), for a fixed input voltage, the strain level on the fiber increases from 178nε at 250Hz to 196nε at 2250Hz, an increase of 10%. For the same frequency range, however, Fig. 10(b) shows a reduction of 80% in the SD. Based on the results shown in Fig. 9(b), an increase in induced strain on the fiber should results in an increase in the SD of the measurement. Therefore, the drop in SD at higher frequencies cannot be associated with the frequency response of the PZT.

All the experimental results obtain in this study exhibit a similar behaviour compared with those of simulation results in reference [18]. The difference in the exact number between the outcome of the numerical model and the experimental result is because in the numerical model noises are not considered.

7. Conclusion

In this study, the effect of four key parameters on an interferometric DAS system were analyzed based on the previous simulation results [18] published by the authors before. The precision of the sensing system as a function of the linewidth of laser and the duration of the probe pulse was assessed. It was shown that the precision of the sensor can be enhanced by increasing the linewidth of laser and reducing the width of the probe pulse. The experimental results showed that the precision of the measurement is also a function of the frequency and amplitude of perturbations. The sensing system has a higher precision when measuring dynamic strains with lower amplitude and higher frequency. The experimental results are in good agreement with the simulation results reported previously [18]. Both the simulation and experimental results presented in this study provide an insight into the operation of DAS systems.

Funding

Engineering and Physical Sciences Research Council (EPSRC) - (EP/N00437X/1); University Natural Science Research Project of Jiangsu Province (16KJB510019); High-Level Training Fund project of Nanjing Xiaozhuang University (2016NXY011).

References

1. J. P. Dakin and C. Lamb, "Distributed fibre optic sensor system," GB patent No. 2222247A (1990).
2. A. H. Hartog, *An Introduction to Distributed Optical Fibre Sensors*, CRC Press (2017).
3. J. C. Juarez, E. W. Maier, K. N. Choi, and H. F. Taylor, "Distributed Fiber-Optic Intrusion Sensor System," J. Lightwave Technol. **23**(6), 2081–2087 (2005).
4. Y. Rao and J. Li, "Distributed intrusion detection based on combination of φ-OTDR and P-OTDR," Proc. The 19th International Conference on Optical Fiber Sensors (OFS-19), Perth, Australia, 700461 (2008).
5. S. Liehr, Y. S. Muanenda, S. Münzenberger, and K. Krebber, "Relative change measurement of physical quantities using dual-wavelength coherent OTDR," Opt. Express **25**(2), 720–729 (2017).
6. A. Masoudi, M. Belal, and T. P. Newson, "A distributed optical fibre dynamic strain sensor based on phase-OTDR," Meas. Sci. Technol. **24**(8), 085204 (2013).
7. X. He, S. Xie, F. Liu, S. Cao, L. Gu, X. Zheng, and M. Zhang, "Multi-event waveform-retrieved distributed optical fiber acoustic sensor using dual-pulse heterodyne phase-sensitive OTDR," Opt. Lett. **42**(3), 442–445 (2017).
8. A. Masoudi and T. P. Newson, "Contributed Review: Distributed optical fibre dynamic strain sensing," Rev. Sci. Instrum. **87**(1), 011501 (2016).
9. A. E. Alekseev, V. S. Vdovenko, B. G. Gorshkov, V. T. Potapov, and D. E. Simikin, "A phase-sensitive optical time-domain reflectometer with dual-pulse phase modulated probe signal," Laser Phys. **24**(11), 115106 (2014).
10. R. I. Crickmore and D. J. Hill, "Traffic sensing and monitoring apparatus," US patent No. 7652245B2, (2010).
11. A. H. Hartog and K. Kader, "Distributed fiber optic sensor system with improved linearity," US patent No. 9170149B2 (2012).
12. Z. Wang, L. Zhang, S. Wang, N. Xue, F. Peng, M. Fan, W. Sun, X. Qian, J. Rao, and Y. Rao, "Coherent Φ-OTDR based on I/Q demodulation and homodyne detection," Opt. Express **24**(2), 853–858 (2016).
13. J. Pastor-Graells, H. F. Martins, A. Garcia-Ruiz, S. Martin-Lopez, and M. Gonzalez-Herraez, "Single-shot distributed temperature and strain tracking using direct detection phase-sensitive OTDR with chirped pulses," Opt. Express **24**(12), 13121–13133 (2016).

Optics EXPRESS

14. D. Chen, Q. Liu, and Z. He, "Phase-detection distributed fiber-optic vibration sensor without fading-noise based on time-gated digital OFDR," Opt. Express **25**(7), 8315–8325 (2017).
15. Z. Yu, Q. Zhang, M. Zhang, H. Dai, J. Zhang, L. Liu, L. Zhang, X. Jin, G. Wang, and G. Qi, "Distributed optical fiber vibration sensing using phase-generated carrier demodulation algorithm, " Appl. Phys. B **124**(5), 84 (2018).
16. G. Fang, T. Xu, S. Feng, and F. Li, "Phase-Sensitive Optical Time Domain Reflectometer Based on Phase-Generated Carrier Algorithm," J. Lightwave Technol. **33**(13), 2811–2816 (2015).
17. A. Masoudi and T. P. Newson, "High spatial resolution distributed optical fiber dynamic strain sensor with enhanced frequency and strain resolution," Opt. Lett. **42**(2), 290–293 (2017).
18. A. Masoudi and T. P. Newson, "Analysis of distributed optical fibre acoustic sensors through numerical modelling," Opt. Express **25**(25), 32021–32040 (2017).
19. W. A. Martins, M. L. R. de Campos, R. da Silva Chaves, C. P. V. Lordelo, A. Ellmauthaler, L. O. Nunes, and D. A. Barfoot, "Communication Models for Distributed Acoustic Sensing for Telemetry," SENS. J. **17**(15), 4677–4688 (2017).
20. M. J. Murray, A. Davis, and B. Redding, "Multimode fiber Φ-OTDR with holographic demodulation," Opt. Express **26**(18), 23019–23030 (2018).
21. M. Chen, A. Masoudi, F. Parmigiani, and G. Brambilla, "Distributed acoustic sensor based on a two-mode fiber," Opt. Express **26**(19), 25399–25407 (2018).
22. Y. Muanenda, C. J. Oton, S. Faralli, and F. Di Pasquale, "A φ-OTDR sensor for high-frequency distributed vibration measurements with minimal post-processing," presented at 19th Italian National Conference on Photonic Technologies, Padua, Italy, 11–18 June 2017.
23. K. De Souza, "Significance of coherent Rayleigh noise in fibre-optic distributed temperature sensing based on spontaneous Brillouin scattering," Meas. Sci. Technol. **17**(5), 1065–1069 (2006).